

Kitaev interaction and possible spin liquid state in CoI_2 and $\text{Co}_{2/3}\text{Mg}_{1/3}\text{I}_2$

Yaozhenghang Ma,^{1,*} Ke Yang,^{2,1,*} Yuxuan Zhou,¹ and Hua Wu^{1,3,4,†}

¹*Laboratory for Computational Physical Sciences (MOE), State Key Laboratory of Surface Physics, and Department of Physics, Fudan University, Shanghai 200433, China*

²*College of Science, University of Shanghai for Science and Technology, Shanghai 200093, China*

³*Shanghai Qi Zhi Institute, Shanghai 200232, China*

⁴*Hefei National Laboratory, Hefei 230088, China*

(Dated: December 30, 2025)

Kitaev materials are of great interest due to their potential in realizing quantum spin liquid (QSL) states and applications in topological quantum computing. In the pursuit of realizing Kitaev QSL, a Mott insulator with strong bond-dependent frustration and weak geometric frustration is highly desirable. Here we explore Kitaev physics in the van der Waals triangular antiferromagnet (AF) CoI_2 , through the spin-orbital states and Wannier function analyses, exact diagonalization and density matrix renormalization group study of the electronic structure and magnetic properties. We find that the high-spin Co^{2+} ion is in the $J_{\text{eff}} = 1/2$ state because of strong spin-orbit coupling, and the weak trigonal elongation and crystal field contribute to the observed weak in-plane magnetic anisotropy. The strong $t_{2g}\text{-}e_g$ hopping via the strong Co 3d-1 5p hybridization gives rise to a strong Kitaev interaction (K_1) at the first nearest neighbors (1NN), and the long Co-Co distance and the weak $t_{2g}\text{-}t_{2g}$ hoppings determine a weak Heisenberg interaction J_1 . The resultant $|K_1/J_1| = 6.63$ confirms a strong bond-dependent frustration, while the geometric frustration due to the 3NN Heisenberg interaction J_3 gets involved, and they all together result in the experimental helical AF order in CoI_2 . We then propose to suppress the J_3 using a partial Mg substitution for Co, and indeed we find that $\text{Co}_{2/3}\text{Mg}_{1/3}\text{I}_2$ has the much reduced geometric frustration but hosts the robust bond-dependent frustration, and thus it would be a promising Kitaev material being so far closest to the QSL state.

Quantum spin liquid (QSL) is one of the most exotic phases in condensed matter physics and has attracted significant interest since it was first conceptualized by Anderson in the 1970s [1, 2]. Considerable efforts have been made to realize quantum spin liquids utilizing geometric frustration on triangular, Kagome, and pyrochlore lattices [3]. Recently, the Kitaev model, which incorporates bond-dependent frustration, has garnered considerable attention due to its Kitaev QSL ground state and Majorana fermion excitations [4]. Jackeli and Khaliullin proposed a method to realize the Kitaev model in d^5 transition metal compounds through the assistance of strong spin-orbit coupling (SOC) [5, 6]. Significant efforts have been devoted to realizing the Kitaev QSL in $4d^5$ and $5d^5$ systems, such as $\alpha\text{-RuCl}_3$ [7–10] and Na_2IrO_3 [11–15]. However, discovering a quantum spin liquid material remains challenging due to the non-negligible Heisenberg interaction. To reduce Heisenberg interaction, Liu *et al* [16] and Sano *et al* [17] proposed that in $3d^7$ systems the contributions to Heisenberg interaction from $t_{2g}\text{-}e_g$ channels and $e_g\text{-}e_g$ channels cancel each other, while the $t_{2g}\text{-}e_g$ channels contribute to a dominant ferromagnetic (FM) Kitaev interaction. Co^{2+} -based $3d^7$ materials, such as $\text{BaCo}_2(\text{AsO}_4)_2$ [18–24], $\text{Na}_3\text{Co}_2\text{SbO}_6$ [25–30] and $\text{Na}_2\text{Co}_2\text{TeO}_6$ [26–28, 31, 32], have been extensively studied in the quest for a dominant Kitaev interaction. However, the study by Liu and Kee reveals that the con-

tributions from $t_{2g}\text{-}t_{2g}$ channels are non-negligible, which boost the otherwise canceled Heisenberg interaction [24].

Very recently, Kim *et al* reported bond-dependent anisotropy in the van der Waals antiferromagnet CoI_2 [33]. CoI_2 contains a triangular network of Co ions with the edge-sharing CoI_6 octahedra, as shown in Fig.1(a). It exhibits a helical antiferromagnetic (AF) order below the Néel temperature $T_N \approx 9$ K [33–35]. The $3d^7 \text{Co}^{2+}$ ion could adopt a $S = 3/2$ high spin state, and the hole on t_{2g} states would contribute to $L = 1$ effective angular momentum. Then the SOC would mix the multiplets into J_{eff} states which are desirable for the Kitaev physics. However, the high spin state may be destabilized, if the energy gain from Hund's coupling is insufficient to counteract the energy cost in octahedral crystal field. In addition, the J_{eff} states from SOC would be disfavored, if the trigonal crystal field is strong enough to destroy the effective $L = 1$ states. Therefore, it is of great interest to investigate whether the Co^{2+} ion is in the $J_{\text{eff}} = 1/2$ Kramers doublet and then produces significant Kitaev interactions. Note also that compared with those previously studied Co^{2+} materials, CoI_2 has a more open structure and larger Co-Co distance which would weaken the Heisenberg interactions. Moreover, the heavy ligand iodine atoms help to enhance the Kitaev interactions [36, 37]. Thus possibly, CoI_2 has dominant Kitaev interactions to achieve QSL.

Based on the above picture, we study the electronic structure and magnetic properties of CoI_2 , using first-principles calculation, Wannier function analysis, exact diagonalization (ED) and density matrix renormalization group (DMRG). Our work confirms that the SOC effect

* Y. M. and K. Y. contributed equally to this work.

† Corresponding author. wuh@fudan.edu.cn

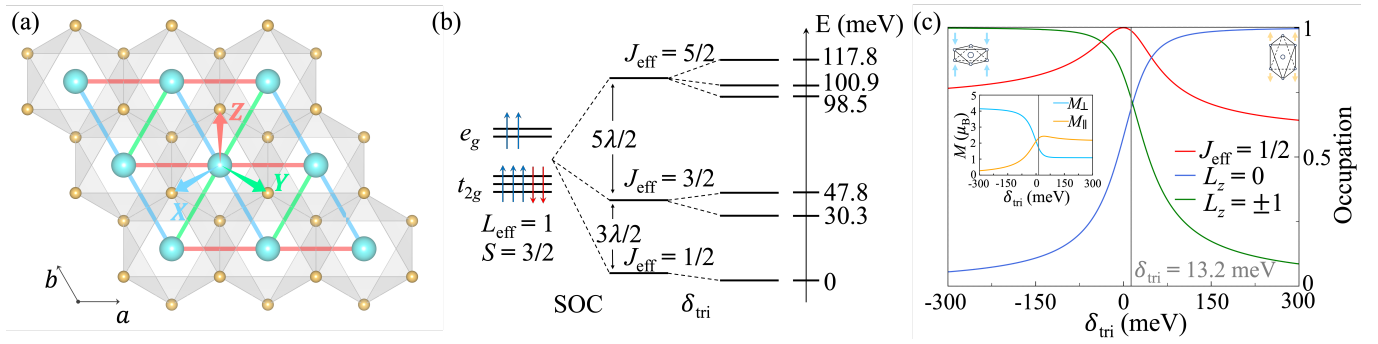


FIG. 1. (a) The *c*-axis view of crystal structure and local basis of CoI_2 . The cyan and yellow balls correspond to Co and I atoms. The local X, Y and Z-axis and the corresponding Kitaev bonds of each axis are indicated by blue, green and red color. (b) Energy splitting of d^7 high spin state under SOC and trigonal crystal field. The excited energy levels are predicted by ED calculation. (c) The occupation number of ground state under different trigonal crystal field. The inset shows out-of-plane (blue curve) and in-plane (yellow curve) magnetic moments under different trigonal crystal field. The gray line denotes trigonal crystal field strength δ of CoI_2 in our calculation.

is stronger than trigonal crystal field, and the electronic ground state is $J_{\text{eff}} = 1/2$ state with weak in-plane magnetic anisotropy. Our study shows that the t_{2g} - e_g channels contribute to a strong Kitaev interaction and the Heisenberg interaction from t_{2g} - t_{2g} channels is effectively suppressed. However, with involvement of the considerably strong antiferromagnetic (AFM) interaction J_3 between third nearest neighbors, the geometric frustration results in the helical magnetic state as experimentally observed. Therefore, we propose a partial Mg substitution for Co to block the J_3 and thus suppress the geometric frustration, and then indeed we find that $\text{Co}_{2/3}\text{Mg}_{1/3}\text{I}_2$ has the overwhelming Kitaev interaction and most closely approaches the Kitaev QSL among several candidates in literature.

To study the electronic structure, we employ a multi-orbital Hubbard model incorporating the five *d* orbitals:

$$H_{\text{one}} = H_{\text{CF}} + H_U + H_{\text{SOC}} \quad (1)$$

where H_{CF} , H_U , and H_{SOC} represent crystal field splitting, Coulomb repulsion and spin-orbit coupling, respectively. The crystal field term for the Co^{2+} ion can be expressed in the basis $\mathbf{c} = (d_{3z^2-r^2}, d_{x^2-y^2}, d_{xz}, d_{yz}, d_{xy})$ as

$$H_{\text{CF}}^{\text{Co}} = \begin{pmatrix} \Delta & 0 & 0 & 0 & 0 \\ 0 & \Delta & 0 & 0 & 0 \\ 0 & 0 & 0 & \delta & \delta \\ 0 & 0 & \delta & 0 & \delta \\ 0 & 0 & \delta & \delta & 0 \end{pmatrix}, \quad (2)$$

where Δ represents the energy difference between the e_g and t_{2g} orbitals, and $\delta_{\text{tri}} = 3\delta$ denotes the splitting between the a_{1g} and e_g^{π} orbitals as derived from the trigonal distortion in the [111] direction of octahedron. The crystal field details are provided in Supplementary Material (SM) I [38]. The Coulomb repulsion is modeled using isotropic Kanamori form [39]. The SOC term is given by

$H_{\text{SOC}} = \lambda \mathbf{L} \cdot \mathbf{S}$, where $\lambda = 26.6$ meV is the atomic SOC strength. We calculated electronic structure and magnetic moment by ED method, as shown in SM II [38].

The magnitude of the t_{2g} - e_g octahedral crystal field splitting (Δ) relative to J_{H} determines the spin state of the Co^{2+} ion. For estimation purposes: the $S = 3/2$ state ($3d^{5\uparrow}t_{2g}^{2\downarrow}$) has a Hund's coupling energy of $-11J_{\text{H}}$ plus $2\Delta_{\text{cf}}$ (the crystal field excitation energy of two electrons in the e_g orbitals), while the $S = 1/2$ state ($t_{2g}^{3\uparrow 3\downarrow}e_g^{1\uparrow}$) has a total stabilization energy of $-9J_{\text{H}}$ plus Δ_{cf} . Thus, the critical condition for a high-spin to low-spin transition is $\Delta_{\text{cf}} > 2J_{\text{H}} = 1.8$ eV. Our Wannier analysis yields a t_{2g} - e_g crystal field splitting of $\Delta = 1.02$ eV, and much smaller than the critical value of 1.8 eV. Therefore, CoI_2 is well stabilized in the high-spin $S = 3/2$ ($3d^{5\uparrow}t_{2g}^{2\downarrow}$) ground state.

In the ($3d^{5\uparrow}t_{2g}^{2\downarrow}$) ground state, the t_{2g} orbitals are not fully occupied, resulting in an unquenched orbital angular momentum with $L_{\text{eff}} = 1$. Consequently, this spin-orbital multiplet comprises 12-degenerate states characterized by ($L_{\text{eff}} = 1, S = 3/2$). When SOC is introduced, these 12-degenerate states further split into $J_{\text{eff}} = 1/2$, $J_{\text{eff}} = 3/2$ and $J_{\text{eff}} = 5/2$ states, as shown in Fig. 1(b). Moreover, under the influence of a trigonal crystal field, the ground state may also be in $L_z = 0$ or $L_z = \pm 1$ state, as shown in Fig. 1(c). Thus, the competition between spin-orbit coupling and trigonal crystal field splitting ultimately determines the intriguing spin-orbital states.

For the Co^{2+} high-spin (HS) state studied here, the spin-orbit coupling strength is typically fixed. Therefore, we vary the trigonal crystal field δ_{tri} and use ED to determine how the ground state evolves. To visualize the changes in the ground state, we project the ED-obtained ground state wavefunctions onto the possible basis states of $J_{\text{eff}} = 1/2$, $L_z = \pm 1$, and $L_z = 0$. As shown in Fig. 1(c), it is evident that when δ_{tri} is less than -150 meV, corresponding to a compressed trigonal distortion, the a_{1g} orbital energy decreases, and the

orbital ground state is $L_z = \pm 1$. Conversely, when δ_{tri} exceeds 150 meV, corresponding to an elongated trigonal distortion, the a_{1g} orbital energy increases, and the orbital ground state becomes $L_z = 0$. Notably, only within the narrow range of $-38 \text{ meV} < \delta_{\text{tri}} < 48 \text{ meV}$ does the system exhibit a well-defined $J_{\text{eff}} = 1/2$ ground state, where the two boundary values are determined by the two crossing points of the three curves of $J_{\text{eff}} = 1/2$, $L_z = \pm 1$, and $L_z = 0$ in Fig. 1(c). To double check accuracy of the obtained ground state, we calculate the expectation value of the total magnetic moment operator, $L + 2S$, from the ground state wavefunction. The results indicate that, when the trigonal field is zero (i.e., under a cubic crystal field), the calculated in-plane and out-of-plane magnetic moments have the equal value of $2.11 \mu_B$, and the associated L  nd g -factor is 4.22. This is in good agreement with the experimental value $g = 4.28$ for Co^{2+} in the cubic MgO lattice [40, 41].

Then, using maximally localized Wannier functions (MLWFs) generated with Wannier90 [42], we obtained the trigonal crystal field splitting of $\delta_{\text{tri}} = 13.2 \text{ meV}$ for the CoI_2 . By projecting the ground-state wavefunction onto the $J_{\text{eff}} = 1/2$ state, we found that the weight reaches as high as 0.98. Note that the small deviation from the pure $J_{\text{eff}} = 1/2$ state results from the trigonal distortion. We also calculated the g -factor for the weak trigonal distortion in CoI_2 : the in-plane g -factor is $g_{||} = 4.62$, while the out-of-plane g -factor is $g_{\perp} = 3.43$. The anisotropic g -factor indicates that the ab -plane is the easy plane for CoI_2 , which is in agreement with experiments [34, 35]. Moreover, due to this weak trigonal distortion, the $J_{\text{eff}} = 3/2$ and $J_{\text{eff}} = 5/2$ excited states further split into five doublets. Our ED calculation gives the excitation energies as $\{30.3, 47.8, 98.5, 100.9, 117.8\}$ meV. The first excitation energy of 30.3 meV is consistent with inelastic neutron scattering data, which reports a value of 35.4 meV [33]. The rest higher-energy excitation states call for experimental verification.

We determined that the electronic structure of CoI_2 is described by $J_{\text{eff}} = 1/2$ picture, and thus the CoI_2 may host the Kitaev interaction. In our calculation, we found the electronic excitation from $J_{\text{eff}} = 1/2$ to $J_{\text{eff}} = 3/2$ requires at least 30.3 meV, which is above the room temperature. Thus, the energy spectrum safely restricts to $J_{\text{eff}} = 1/2$ states in our work. And magnetic structure of CoI_2 can be studied within $J_{\text{eff}} = 1/2$ Kramers doublet framework using a low-energy $S = 1/2$ spin Hamiltonian.

To study the magnetic exchange parameters, we employ a multi-orbital Hubbard model including two Co^{2+} sites:

$$H = H_{\text{one}} + H_t, \quad (3)$$

where H_{one} and H_t represent one-site Hamiltonian term of each Co^{2+} and hopping terms between two Co^{2+} , respectively. The Z bond hopping matrix between sites Co_i and Co_j can be expressed in the basis $\mathbf{c} =$

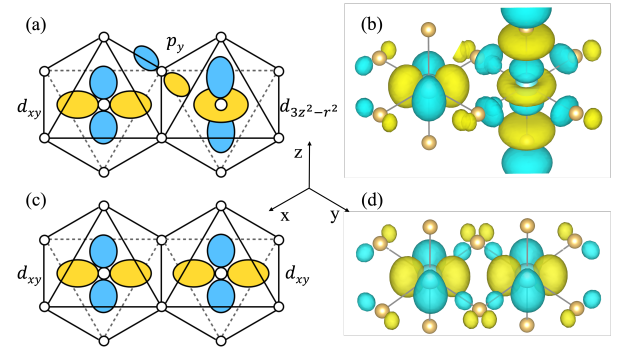


FIG. 2. The schematic diagram of (a) the dominant t_{2g} - e_g hopping: indirect hopping between d_{xy} and $d_{3z^2-r^2}$ orbitals and (c) the dominant t_{2g} - t_{2g} hopping: direct hopping between d_{xy} orbitals. The corresponding Wannier functions are plotted in (b) and (d).

$(d_{3z^2-r^2}, d_{x^2-y^2}, d_{xz}, d_{yz}, d_{xy})$ as

$$H_t^{(ij)} = \begin{pmatrix} t_5 & 0 & 0 & 0 & t_6 \\ 0 & t_4 & 0 & 0 & 0 \\ 0 & 0 & t_1 & t_2 & 0 \\ 0 & 0 & t_2 & t_1 & 0 \\ t_6 & 0 & 0 & 0 & t_3 \end{pmatrix}, \quad (4)$$

where t_{1-6} are the hopping terms allowed by C_{2v} symmetry [24]. These hopping terms and all other non-zero terms due to the lowered C_s symmetry are obtained through MLWFs, as shown in SM III [38]. The magnetic properties are studied within a low-energy spin Hamiltonian, in which the $J_{\text{eff}} = 1/2$ Kramers doublets are mapped into $S = 1/2$ pseudospin. For the triangular and hexagonal lattice, the general spin Hamiltonian is given by

$$H = \sum_{ij} JS_i \cdot S_j + KS_i^{\gamma} S_j^{\gamma} + \Gamma \left(S_i^{\alpha} S_j^{\beta} + S_i^{\beta} S_j^{\alpha} \right) + \Gamma' \left(S_i^{\gamma} S_j^{\alpha} + S_i^{\gamma} S_j^{\beta} + S_i^{\alpha} S_j^{\gamma} + S_i^{\beta} S_j^{\gamma} \right) \quad (5)$$

where $\{\alpha, \beta, \gamma\} = \{x, y, z\}$, $\{y, z, x\}$, and $\{z, x, y\}$ for the Z , X , and Y bonds, respectively. The spin Hamiltonian is obtained by solving the multi-orbital Hubbard model, and the details of calculation are shown in SM IV [38].

For CoI_2 , the interaction between first nearest neighbors is the most important term, and the strongest hopping channel is $t_6 = 177.1 \text{ meV}$, as shown in Eq. S17 of SM [38]. As shown in Fig. 2(a)-(b), the strongest t_6 term is indirect hopping term between t_{2g} and e_g orbitals, which makes difference with other Co^{2+} materials. And unlike others, in CoI_2 the t_{2g} - t_{2g} hopping channel, as illustrated in Fig. 2(c)-(d), is relative weak with value $t_3 = -44.1 \text{ meV}$ in Eq. S17 of SM [38]. The Co-Co distance 3.87   in CoI_2 is much longer than 2.89   in $\text{BaCo}_2(\text{AsO}_4)_2$ [23] and 2.80   in $\text{BaCo}_2(\text{PO}_4)_2$ [43]. The longer bond suppresses the direct hopping channels, leading to relative enhancement of indirect hopping channels. Additionally, CoI_2 has the heavier ligand iodine,

TABLE I. First, second and third nearest neighbor magnetic interactions in meV for CoI_2 ($\text{Co}_{2/3}\text{Mg}_{1/3}\text{I}_2$).

	J	K	Γ	Γ'
1NN	0.63 (0.89)	-4.17 (-3.15)	-0.04 (-0.07)	0.06 (0.27)
2NN	-0.15 (-0.21)	-0.56 (-0.32)	0.40 (0.04)	-0.14 (0.02)
3NN	2.16 (0.53)	-0.06 (0.01)	0.38 (0.01)	0.30 (0.06)

and the strong interaction between Co^{2+} $3d$ orbitals and I^- $5p$ orbitals enhances the p -orbital-mediated hopping process t_6 . As shown in Table S1 of SM[38], the dominant t_6 channel contributes to a strong FM Kitaev interaction $K = -4.73$ meV and a weak AFM Heisenberg interaction $J = 0.81$ meV, leading to the dominant Kitaev interaction in CoI_2 .

For triangular [3] and hexagonal lattices [23], the geometric frustration associated with second and third nearest neighbors' interaction attracts considerable attention, and it turns out to be important as seen below. The complex competition between geometric frustration and bond dependent frustration determines the magnetic ground state. As shown in Table S1 and Fig. S9 of SM [38], the geometric frustration arising from second nearest neighbors is negligible compared to that originating from third nearest neighbors, where the dominant channel $t_2 = -39.1$ meV associated with second nearest neighbors only contributes $J = -0.24$ meV while the principle channel $t_4 = 92.0$ meV involving in third nearest neighbors yields a significantly larger contribution with $J = 1.9$ meV. Thus the AFM Heisenberg interaction between third nearest neighbors is the the primary contributor to geometric frustration.

Then we solved the multi-orbital Hubbard model containing all hopping channels and obtained the exchange parameters in the spin Hamiltonian, shown in Table I. As proposed above, we found a strong FM Kitaev interaction $K_1 = -4.17$ meV and a relative weak AFM Heisenberg interaction $J_1 = 0.63$ meV. The bond-dependent frustration in CoI_2 is remarkable, with the $|K_1|/|J_1|$ ratio equal to 6.63, while the ratio in $\text{BaCo}_2(\text{AsO}_4)_2$ is only 0.06 [24]. Meanwhile, the strong AFM Heisenberg interaction $J_3 = 2.16$ meV induces strong geometric frustration.

The existence of bond-dependent and geometric frustration suggests that the magnetic ground state is determined by their complex competition. Here, we used DMRG method to calculate the phase diagram with and without J_3 on a 6×6 triangular lattice. The energy values in our DMRG calculation without J_3 are consistent with those derived from ED calculation on 6×4 triangular lattice in Fig. 10 of reference [44], which corroborates the accuracy of our DMRG calculation. To simplify the model Hamiltonian, we included the three dominant interactions in phase diagram, Heisenberg interaction J_1 , Kitaev interaction K_1 and Heisenberg interaction J_3 . As shown in Fig. 3, in our calculations, we set $J_1 = A \cos \varphi$ and $K_1 = A \sin \varphi$ using the angle parameter $\varphi \in [0, 2\pi]$, with $A = \sqrt{K_1^2 + J_1^2}$.

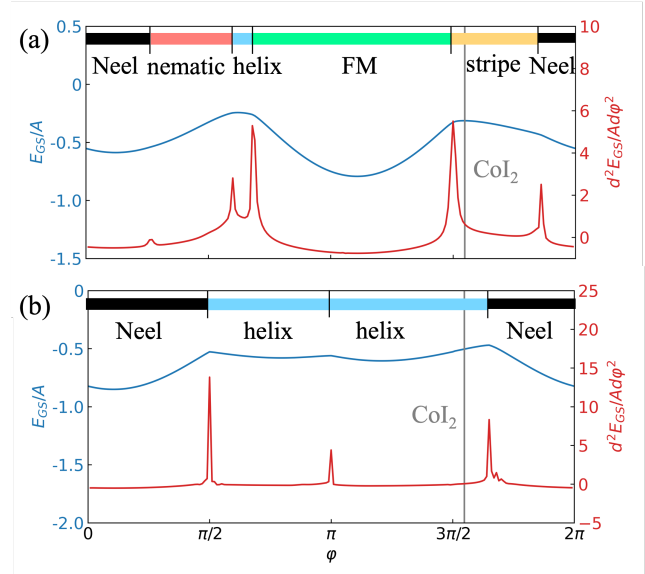


FIG. 3. The DMRG results and phase diagrams of Kitaev-Heisenberg model on triangular lattice (a) without J_3 and (b) with J_3 . The ground state energy E_{gs}/A per site and its second derivative $d^2E_{\text{gs}}/Ad\varphi^2$ are indicated by blue and red line respectively.

For the parameter space without J_3 , the phase diagram is divided into five regions, as shown in Fig. 3(a). For a pure Heisenberg model, the ground state is either a FM state or a 120° Néel AFM state. When the Kitaev interaction is included, the bond-dependent frustration induces three new phases: helical AFM, nematic, and stripe AFM. In total, the ground state turns out to be the stripe AFM but not the experimental helical AFM. However, in the parameter space with J_3 , the bond-dependent frustration is suppressed by geometric frustration, leaving only the 120° Néel AFM state and the helical AFM state, as shown in Fig. 3(b). Now the ground state becomes the helical AFM state in agreement with the experiment [33]. Therefore, both the FM Kitaev interaction K_1 and the AFM Heisenberg interaction J_3 play a major role in deterring the experimental helical AFM state of CoI_2 [33].

The bond-dependent frustration promotes a Kitaev QSL state when the Kitaev interaction dominates, while the geometric frustration arising from longer-range Heisenberg terms tends to stabilize non-QSL orders such as the helical AFM phase. To explore the bond-dependent QSL, we propose $\text{Co}_{2/3}\text{Mg}_{1/3}\text{I}_2$ (with a partial Mg substitution for Co, see Fig. 4(a)) to block the J_3 interaction via intermediate Mg ion. Thus, the suppression of the J_3 -driven geometric frustration would unmask the bond-dependent frustration. Note that the induced trigonal distortion remains small, as Mg^{2+} has similar ionic size of 0.72 Å to that of 0.745 Å for Co^{2+} [46].

For $\text{Co}_{2/3}\text{Mg}_{1/3}\text{I}_2$, we performed another set of DFT, MLWFs and ED calculations. Here the calculated octahedral $t_{2g}-e_g$ splitting of 0.99 eV (after structural re-

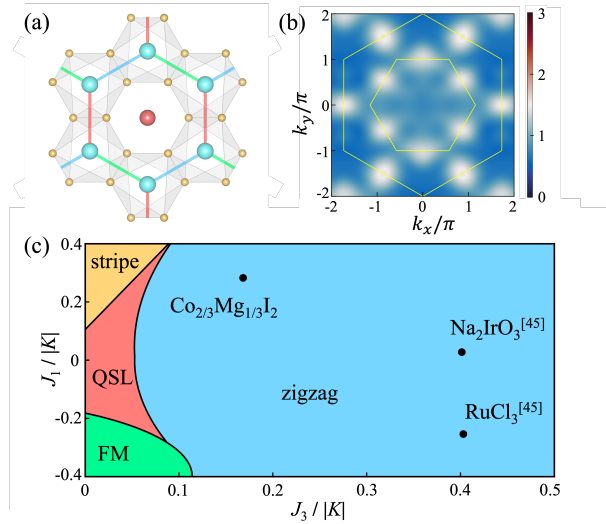


FIG. 4. (a) The crystal structure of $\text{Co}_{2/3}\text{Mg}_{1/3}\text{I}_2$. The cyan, red and yellow balls represent Co, Mg and I atoms respectively. (b) Magnetic structure factor $S(q)$ of $\text{Co}_{2/3}\text{Mg}_{1/3}\text{I}_2$ with 30% J_3 . The colormap is limited to the range of 0 to the maximum value $S(q)_{\text{max}}$ of zigzag and stripe order as shown in Fig. S11 of SM [38]. (c) Phase diagram for FM Kitaev interaction $K < 0$ by ED. The exchange parameters of Na_2IrO_3 and RuCl_3 are from Ref. [45].

laxation) is almost the same as that of 1.02 eV in CoI_2 , and the trigonal crystal field splitting remains tiny (here only 4.5 meV), thus resulting in the robust $J_{\text{eff}} = 1/2$ ground state in $\text{Co}_{2/3}\text{Mg}_{1/3}\text{I}_2$. The interaction between first nearest neighbors remains dominated by the t_6 term, while the third nearest neighbors' contributions are notably suppressed, as seen in Table I. Now the $|K_1|/|J_3|$ ratio increases drastically from 1.9 of CoI_2 to 5.9 of $\text{Co}_{2/3}\text{Mg}_{1/3}\text{I}_2$. To study magnetic structure and phase transitions, we calculated the magnetic structure factor $S(q)$ and the phase diagram. As shown in Fig. 4(b), with the suppressed J_3 interaction, $S(q)$ is diffusive with soft peak at M -point in first and second Brillouin zones. As comparison, the stripe order and zigzag order display sharp features at M -point in second and first Brillouin zone respectively, as shown in SM [38]. Although

the residual geometric frustration in $\text{Co}_{2/3}\text{Mg}_{1/3}\text{I}_2$ somewhat prohibits the QSL state, as shown in Fig. 4(c), $\text{Co}_{2/3}\text{Mg}_{1/3}\text{I}_2$ is already closest to the Kitaev QSL region and would provide a better platform for realizing Kitaev QSL than other candidates such as Na_2IrO_3 and RuCl_3 . Then the Kitaev QSL state may readily be realized in $\text{Co}_{2/3}\text{Mg}_{1/3}\text{I}_2$ with the help of a magnetic field [47] or high pressure [48]. Indeed, our calculations including a Zeeman term find that the Kitaev QSL phase emerges within the intermediate magnetic field of 2.0–4.3 T, as seen in Section V of SM [38].

In summary, we demonstrate that CoI_2 is a potential Kitaev material, using crystal field analysis, DFT calculations, Wannier function analysis, ED and DMRG calculations. Our results show that the high spin Co^{2+} is in the isotropic $J_{\text{eff}} = \frac{1}{2}$ ground state, while the small trigonal distortion induces a weak in-plane anisotropy with $g_{||} = 4.62$ (vs $g_{\perp} = 3.43$). The long Co-Co distance weakens the t_{2g} - t_{2g} hopping and thus reduces the corresponding Heisenberg AFM couplings, but the strong Co-I hybridization enhances the t_{2g} - e_g hopping and produces strong FM Kitaev interaction. Both the Kitaev interaction and the geometric frustration from AFM J_3 determine the experimental helical magnetic state of CoI_2 . We propose a partial Mg substitution for Co to suppress the geometric frustration, and indeed find that the resultant $\text{Co}_{2/3}\text{Mg}_{1/3}\text{I}_2$ has much weakened geometric frustration but the robust bond dependent frustration. As a result, the overwhelming Kitaev interaction renders $\text{Co}_{2/3}\text{Mg}_{1/3}\text{I}_2$ closest to QSL among several candidate materials. Such prediction may be worth a prompt experimental study.

ACKNOWLEDGEMENTS

This work was supported by National Natural Science Foundation of China (Grants No. 12174062, No. 12241402, and No. 12574127), and by Quantum Science and Technology-National Science and Technology Major Project (2024ZD0300102). Y. Ma and K. Yang contributed equally to this work.

[1] P. W. Anderson, Resonating valence bonds: A new kind of insulator?, *Mater. Res. Bull.* **8**, 153 (1973).

[2] P. Fazekas and P. W. Anderson, On the ground state properties of the anisotropic triangular antiferromagnet, *Philos. Mag.* **30**, 423 (1974).

[3] L. Balents, Spin liquids in frustrated magnets, *Nature* **464**, 199 (2010).

[4] A. Kitaev, Anyons in an exactly solved model and beyond, *Ann. Phys. (N.Y.)* **321**, 2 (2006).

[5] G. Jackeli and G. Khaliullin, Mott insulators in the strong spin-orbit coupling limit: From Heisenberg to a quantum compass and Kitaev models, *Phys. Rev. Lett.* **102**, 017205 (2009).

[6] H. Takagi, T. Takayama, G. Jackeli, G. Khaliullin, and S. E. Nagler, Concept and realization of Kitaev quantum spin liquids, *Nat. Rev. Phys.* **1**, 264 (2019).

[7] K. W. Plumb, J. P. Clancy, L. J. Sandilands, V. V. Shankar, Y. F. Hu, K. S. Burch, H.-Y. Kee, and Y.-J. Kim, α - RuCl_3 : A spin-orbit assisted Mott insulator on a honeycomb lattice, *Phys. Rev. B* **90**, 041112 (2014).

[8] L. J. Sandilands, Y. Tian, K. W. Plumb, Y.-J. Kim, and K. S. Burch, Scattering continuum and possible fractionalized excitations in α - RuCl_3 , *Phys. Rev. Lett.* **114**, 147201 (2015).

[9] H.-S. Kim, V. S. V., A. Catuneanu, and H.-Y. Kee, Kitaev magnetism in honeycomb RuCl_3 with intermediate spin-orbit coupling, *Phys. Rev. B* **91**, 241110 (2015).

[10] A. Banerjee, C. A. Bridges, J.-Q. Yan, A. A. Aczel, L. Li, M. B. Stone, G. E. Granroth, M. D. Lumsden, Y. Yiu, J. Knolle, S. Bhattacharjee, D. L. Kovrizhin, R. Moessner, D. A. Tennant, D. G. Mandrus, and S. E. Nagler, Proximate Kitaev quantum spin liquid behaviour in a honeycomb magnet, *Nat. Mater.* **15**, 733 (2016).

[11] J. Chaloupka, G. Jackeli, and G. Khaliullin, Kitaev-Heisenberg model on a honeycomb lattice: Possible exotic phases in iridium oxides A_2IrO_3 , *Phys. Rev. Lett.* **105**, 027204 (2010).

[12] X. Liu, T. Berlijn, W.-G. Yin, W. Ku, A. Tsvelik, Y.-J. Kim, H. Gretarsson, Y. Singh, P. Gegenwart, and J. P. Hill, Long-range magnetic ordering in Na_2IrO_3 , *Phys. Rev. B* **83**, 220403 (2011).

[13] F. Ye, S. Chi, H. Cao, B. C. Chakoumakos, J. A. Fernandez-Baca, R. Custelcean, T. F. Qi, O. B. Korneta, and G. Cao, Direct evidence of a zigzag spin-chain structure in the honeycomb lattice: A neutron and x-ray diffraction investigation of single-crystal Na_2IrO_3 , *Phys. Rev. B* **85**, 180403 (2012).

[14] J. Chaloupka, G. Jackeli, and G. Khaliullin, Zigzag magnetic order in the iridium oxide Na_2IrO_3 , *Phys. Rev. Lett.* **110**, 097204 (2013).

[15] S. Hwan Chun, J.-W. Kim, J. Kim, H. Zheng, C. C. Stoumpos, C. D. Malliakas, J. F. Mitchell, K. Mehlawat, Y. Singh, Y. Choi, T. Gog, A. Al-Zein, M. M. Sala, M. Krisch, J. Chaloupka, G. Jackeli, G. Khaliullin, and B. J. Kim, Direct evidence for dominant bond-directional interactions in a honeycomb lattice iridate Na_2IrO_3 , *Nat. Phys.* **11**, 462 (2015).

[16] H. Liu and G. Khaliullin, Pseudospin exchange interactions in d^7 cobalt compounds: Possible realization of the Kitaev model, *Phys. Rev. B* **97**, 014407 (2018).

[17] R. Sano, Y. Kato, and Y. Motome, Kitaev-Heisenberg Hamiltonian for high-spin d^7 Mott insulators, *Phys. Rev. B* **97**, 014408 (2018).

[18] R. Zhong, T. Gao, N. P. Ong, and R. J. Cava, Weak-field induced nonmagnetic state in a Co-based honeycomb, *Sci. Adv.* **6**, eaay6953 (2020).

[19] W. Chen, X. Li, Z. Hu, Z. Hu, L. Yue, R. Sutarto, F. He, K. Iida, K. Kamazawa, W. Yu, X. Lin, and Y. Li, Spin-orbit phase behavior of $\text{Na}_2\text{Co}_2\text{TeO}_6$ at low temperatures, *Phys. Rev. B* **103**, L180404 (2021).

[20] S. Das, S. Voleti, T. Saha-Dasgupta, and A. Paramekanti, XY magnetism, Kitaev exchange, and long-range frustration in the $J_{\text{eff}} = \frac{1}{2}$ honeycomb cobaltates, *Phys. Rev. B* **104**, 134425 (2021).

[21] P. A. Maksimov, A. V. Ushakov, Z. V. Pchelkina, Y. Li, S. M. Winter, and S. V. Streltsov, Ab initio guided minimal model for the "Kitaev" material $\text{BaCo}_2(\text{AsO}_4)_2$: Importance of direct hopping, third-neighbor exchange, and quantum fluctuations, *Phys. Rev. B* **106**, 165131 (2022).

[22] S. M. Winter, Magnetic couplings in edge-sharing high-spin $d7$ compounds, *J. Phys. Mater.* **5**, 045003 (2022).

[23] T. Halloran, F. Desrochers, E. Z. Zhang, T. Chen, L. E. Chern, Z. Xu, B. Winn, M. Graves-Brook, M. B. Stone, A. I. Kolesnikov, Y. Qiu, R. Zhong, R. Cava, Y. B. Kim, and C. Broholm, Geometrical frustration versus Kitaev interactions in $\text{BaCo}_2(\text{AsO}_4)_2$, *Proc. Natl. Acad. Sci. U.S.A.* **120**, e2215509119 (2023).

[24] X. Liu and H.-Y. Kee, Non-Kitaev versus Kitaev honeycomb cobaltates, *Phys. Rev. B* **107**, 054420 (2023).

[25] H. Liu, J. Chaloupka, and G. Khaliullin, Kitaev spin liquid in $3d$ transition metal compounds, *Phys. Rev. Lett.* **125**, 047201 (2020).

[26] M. Songvilay, J. Robert, S. Petit, J. A. Rodriguez-Rivera, W. D. Ratcliff, F. Damay, V. Balédent, M. Jiménez-Ruiz, P. Lejay, E. Pachoud, A. Hadj-Azzem, V. Simonet, and C. Stock, Kitaev interactions in the Co honeycomb anti-ferromagnets $\text{Na}_3\text{Co}_2\text{SbO}_6$ and $\text{Na}_2\text{Co}_2\text{TeO}_6$, *Phys. Rev. B* **102**, 224429 (2020).

[27] C. Kim, J. Jeong, G. Lin, P. Park, T. Masuda, S. Asai, S. Itoh, H.-S. Kim, H. Zhou, J. Ma, and J.-G. Park, Antiferromagnetic Kitaev interaction in $j_{\text{eff}} = 1/2$ cobalt honeycomb materials $\text{Na}_3\text{Co}_2\text{SbO}_6$ and $\text{Na}_2\text{Co}_2\text{TeO}_6$, *J. Phys.: Condens. Matter* **34**, 045802 (2021).

[28] A. L. Sanders, R. A. Mole, J. Liu, A. J. Brown, D. Yu, C. D. Ling, and S. Rachel, Dominant Kitaev interactions in the honeycomb materials $\text{Na}_3\text{Co}_2\text{SbO}_6$ and $\text{Na}_2\text{Co}_2\text{TeO}_6$, *Phys. Rev. B* **106**, 014413 (2022).

[29] X. Li, Y. Gu, Y. Chen, V. O. Garlea, K. Iida, K. Kamazawa, Y. Li, G. Deng, Q. Xiao, X. Zheng, Z. Ye, Y. Peng, I. A. Zaliznyak, J. M. Tranquada, and Y. Li, Giant magnetic in-plane anisotropy and competing instabilities in $\text{Na}_3\text{Co}_2\text{SbO}_6$, *Phys. Rev. X* **12**, 041024 (2022).

[30] E. Vavilova, T. Vasilchikova, A. Vasiliev, D. Mikhailova, V. Nalbandyan, E. Zvereva, and S. V. Streltsov, Magnetic phase diagram and possible Kitaev-like behavior of the honeycomb-lattice antimonate $\text{Na}_3\text{Co}_2\text{SbO}_6$, *Phys. Rev. B* **107**, 054411 (2023).

[31] G. Lin, J. Jeong, C. Kim, Y. Wang, Q. Huang, T. Masuda, S. Asai, S. Itoh, G. Günther, M. Russina, Z. Lu, J. Sheng, L. Wang, J. Wang, G. Wang, Q. Ren, C. Xi, W. Tong, L. Ling, Z. Liu, L. Wu, J. Mei, Z. Qu, H. Zhou, X. Wang, J.-G. Park, Y. Wan, and J. Ma, Field-induced quantum spin disordered state in spin-1/2 honeycomb magnet $\text{Na}_2\text{Co}_2\text{TeO}_6$, *Nat. Commun.* **12**, 5559 (2021).

[32] W. Yao, K. Iida, K. Kamazawa, and Y. Li, Excitations in the ordered and paramagnetic states of honeycomb magnet $\text{Na}_2\text{Co}_2\text{TeO}_6$, *Phys. Rev. Lett.* **129**, 147202 (2022).

[33] C. Kim, S. Kim, P. Park, T. Kim, J. Jeong, S. Ohira-Kawamura, N. Murai, K. Nakajima, A. L. Chernyshev, M. Mourigal, S.-J. Kim, and J.-G. Park, Bond-dependent anisotropy and magnon decay in cobalt-based Kitaev triangular antiferromagnet, *Nat. Phys.* **19**, 1624 (2023).

[34] S. Kuindersma, J. Sanchez, and C. Haas, Magnetic and structural investigations on NiI_2 and CoI_2 , *Physica B+C* **111**, 231 (1981).

[35] T. Kurumaji, S. Seki, S. Ishiwata, H. Murakawa, Y. Kaneko, and Y. Tokura, Magnetoelectric responses induced by domain rearrangement and spin structural change in triangular-lattice helimagnets NiI_2 and CoI_2 , *Phys. Rev. B* **87**, 014429 (2013).

[36] C. Xu, J. Feng, H. Xiang, and L. Bellaiche, Interplay between Kitaev interaction and single ion anisotropy in ferromagnetic CrI_3 and CrGeTe_3 monolayers, *npj Comput. Mater.* **4**, 57 (2018).

[37] C. Xu, J. Feng, M. Kawamura, Y. Yamaji, Y. Nahas, S. Prokhorenko, Y. Qi, H. Xiang, and L. Bellaiche, Possible Kitaev quantum spin liquid state in 2D materials with $S = 3/2$, *Phys. Rev. Lett.* **124**, 087205 (2020).

[38] See Supplemental Material for more details on (I) crystal field and spin state, (II) occupation and magnetic moment results, (III) Wannier function results, (IV) the ex-

change parameters and (V) magnetic structure. The Supplemental Material also contains Refs. [4, 39, 42, 45, 49–53].

[39] A. Georges, L. de’ Medici, and J. Mravlje, Strong correlations from Hund’s coupling, *Annu. Rev. Condens. Matter Phys.* **4**, 137 (2013).

[40] W. Low and R. Rubins, Electron spin resonance in the cubic crystalline field of calcium oxide, *Phys. Lett.* **1**, 316 (1962).

[41] A. Abragam and B. Bleaney, *Electron paramagnetic resonance of transition ions* (Oxford University Press, 2012).

[42] A. A. Mostofi, J. R. Yates, Y.-S. Lee, I. Souza, D. Vanderbilt, and N. Marzari, Wannier90: A tool for obtaining maximally-localised Wannier functions, *Comput. Phys. Commun.* **178**, 685 (2008).

[43] H. S. Nair, J. M. Brown, E. Coldren, G. Hester, M. P. Gelfand, A. Podlesnyak, Q. Huang, and K. A. Ross, Short-range order in the quantum XXZ honeycomb lattice material BaCo₂(PO₄)₂, *Phys. Rev. B* **97**, 134409 (2018).

[44] M. Becker, M. Hermanns, B. Bauer, M. Garst, and S. Trebst, Spin-orbit physics of $j = \frac{1}{2}$ Mott insulators on the triangular lattice, *Phys. Rev. B* **91**, 155135 (2015).

[45] S. M. Winter, Y. Li, H. O. Jeschke, and R. Valentí, Challenges in design of Kitaev materials: Magnetic interactions from competing energy scales, *Phys. Rev. B* **93**, 214431 (2016).

[46] R. D. Shannon, Revised effective ionic radii and systematic studies of interatomic distances in halides and chalcogenides, *Acta Crystallogr. A* **32**, 751 (1976).

[47] J. S. Gordon, A. Catuneanu, E. S. Sørensen, and H.-Y. Kee, Theory of the field-revealed Kitaev spin liquid, *Nat. Commun.* **10**, 2470 (2019).

[48] Q. Stahl, T. Ritschel, G. Garbarino, F. Cova, A. Isaeva, T. Doert, and J. Geck, Pressure-tuning of α -RuCl₃ towards a quantum spin liquid, *Nat. Commun.* **15**, 8142 (2024).

[49] G. Kresse and J. Hafner, Ab initio molecular dynamics for liquid metals, *Phys. Rev. B* **47**, 558 (1993).

[50] J. P. Perdew, J. A. Chevary, S. H. Vosko, K. A. Jackson, M. R. Pederson, D. J. Singh, and C. Fiolhais, Atoms, molecules, solids, and surfaces: Applications of the generalized gradient approximation for exchange and correlation, *Phys. Rev. B* **46**, 6671 (1992).

[51] M. A. McGuire, Crystal and magnetic structures in layered, transition metal dihalides and trihalides, *Crystals* **7**, 121 (2017).

[52] S. R. White, Density matrix formulation for quantum renormalization groups, *Phys. Rev. Lett.* **69**, 2863 (1992).

[53] M. Fishman, S. White, and E. M. Stoudenmire, The ITensor software library for tensor network calculations, *SciPost Phys. Codebases* , 4 (2022).

SUPPLEMENTAL MATERIAL FOR "KITAEV INTERACTION AND POSSIBLE SPIN LIQUID STATE IN COI₂ AND CO_{2/3}MG_{1/3}I₂"

I. Crystal field and spin state of CoI₂

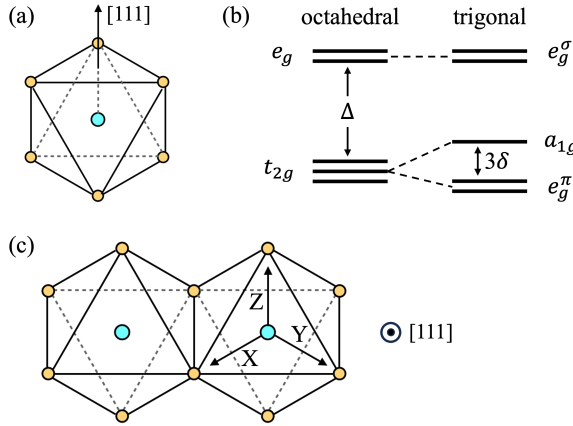


Fig. S1. (a) Schematic diagram of local CoI₆ octahedron. (b) Splitting of energy levels of Co d orbitals under local octahedral crystal field and global trigonal crystal field. Under octahedral crystal field, the degenerate d orbitals split into *t*_{2g} orbitals and *e*_g orbitals with energy difference Δ . The trigonal distortion along [111] direction further split *t*_{2g} orbitals into *e*_g^π and *a*_{1g} orbitals with energy difference 3δ . (c) Structure and coordinate of two-site model of Z bond.

The crystal structure of CoI₂ belongs to *P* $\bar{3}m1$ space group. The edge-sharing CoI₆ octahedrons form a triangular network, with the [111] direction of the octahedra aligned along the global z-axis of the van der Waals layer. As shown in Fig. S1, the trigonal distortion along the [111] direction of the octahedra splits the degenerate *t*_{2g} shells into *a*_{1g} and *e*_g^π sub-shells. For trigonal elongation ($\delta > 0$), the *e*_g^π states lie below the *a*_{1g} state, whereas for trigonal compression ($\delta < 0$), the *a*_{1g} state is favored. Through exact diagonalization (ED), we can find the energy difference between *a*_{1g} and *e*_g^π states is 3δ , where δ is off-diagonal term in crystal field matrix. The spin-orbit coupling (SOC) term, however, has different effect on orbital state. For strong trigonal crystal field limit, the SOC is treated as a perturbation, as illustrated in right part of Fig. S2. In the $\delta > 0$ crystal field, the two minor spins occupy the lower *e*_g^π orbitals, resulting in a quenched orbital moment ground state ($L_z = 0$). However, in strong SOC limit, as illustrated in left part of Fig. S2, the high spin state splits into *J*_{eff} states, and the trigonal crystal field is treated as perturbation to further split *J*_{eff} states. The wavefunctions of 12 *J*_{eff} states are listed in Eq. S1-S12. The left side of equals sign represents *J*_{eff} state $|J, j_z\rangle$, while the right side represents $|S_z, L_z\rangle$. To study d^7 *J*_{eff} states, we must include multi-electron effect in our model with help of ED, as for example the $|S_z, L_z\rangle = |\frac{1}{2}, 0\rangle$ and the $|S_z, L_z\rangle = |\frac{3}{2}, 0\rangle$

are in-distinguishable in density functional theory (DFT) calculation.

$$\left| \frac{1}{2}, -\frac{1}{2} \right\rangle = \frac{1}{\sqrt{6}} \left| \frac{1}{2}, -1 \right\rangle - \frac{1}{\sqrt{3}} \left| -\frac{1}{2}, 0 \right\rangle + \frac{1}{\sqrt{2}} \left| -\frac{3}{2}, 1 \right\rangle \quad (\text{S6})$$

$$\left| \frac{1}{2}, \frac{1}{2} \right\rangle = \frac{1}{\sqrt{2}} \left| \frac{3}{2}, -1 \right\rangle - \frac{1}{\sqrt{3}} \left| \frac{1}{2}, 0 \right\rangle + \frac{1}{\sqrt{6}} \left| -\frac{1}{2}, 1 \right\rangle \quad (\text{S7})$$

$$\left| \frac{3}{2}, -\frac{3}{2} \right\rangle = -\sqrt{\frac{2}{5}} \left| -\frac{1}{2}, -1 \right\rangle + \sqrt{\frac{3}{5}} \left| -\frac{3}{2}, 0 \right\rangle \quad (\text{S8})$$

$$\left| \frac{3}{2}, -\frac{1}{2} \right\rangle = -\sqrt{\frac{8}{15}} \left| \frac{1}{2}, -1 \right\rangle + \sqrt{\frac{1}{15}} \left| -\frac{1}{2}, 0 \right\rangle + \sqrt{\frac{2}{5}} \left| -\frac{3}{2}, 1 \right\rangle \quad (\text{S9})$$

$$\left| \frac{3}{2}, \frac{1}{2} \right\rangle = -\sqrt{\frac{2}{5}} \left| \frac{3}{2}, -1 \right\rangle - \sqrt{\frac{1}{15}} \left| \frac{1}{2}, 0 \right\rangle + \sqrt{\frac{8}{15}} \left| -\frac{1}{2}, 1 \right\rangle \quad (\text{S10})$$

$$\left| \frac{3}{2}, \frac{3}{2} \right\rangle = -\sqrt{\frac{3}{5}} \left| \frac{3}{2}, 0 \right\rangle + \sqrt{\frac{2}{5}} \left| \frac{1}{2}, 1 \right\rangle \quad (\text{S11})$$

$$\left| \frac{5}{2}, -\frac{5}{2} \right\rangle = \left| -\frac{3}{2}, -1 \right\rangle \quad (\text{S12})$$

$$\left| \frac{5}{2}, -\frac{3}{2} \right\rangle = \sqrt{\frac{3}{5}} \left| -\frac{1}{2}, -1 \right\rangle + \sqrt{\frac{2}{5}} \left| -\frac{3}{2}, 0 \right\rangle \quad (\text{S13})$$

$$\left| \frac{5}{2}, -\frac{1}{2} \right\rangle = \sqrt{\frac{3}{10}} \left| \frac{1}{2}, -1 \right\rangle + \sqrt{\frac{3}{5}} \left| -\frac{1}{2}, 0 \right\rangle + \sqrt{\frac{1}{10}} \left| -\frac{3}{2}, 1 \right\rangle \quad (\text{S14})$$

$$\left| \frac{5}{2}, \frac{1}{2} \right\rangle = \sqrt{\frac{1}{10}} \left| \frac{3}{2}, -1 \right\rangle + \sqrt{\frac{3}{5}} \left| \frac{1}{2}, 0 \right\rangle + \sqrt{\frac{3}{10}} \left| -\frac{1}{2}, 1 \right\rangle \quad (\text{S15})$$

$$\left| \frac{5}{2}, \frac{3}{2} \right\rangle = \sqrt{\frac{2}{5}} \left| \frac{3}{2}, 0 \right\rangle + \sqrt{\frac{3}{5}} \left| \frac{1}{2}, 1 \right\rangle \quad (\text{S16})$$

$$\left| \frac{5}{2}, \frac{5}{2} \right\rangle = \left| \frac{3}{2}, 1 \right\rangle \quad (\text{S17})$$

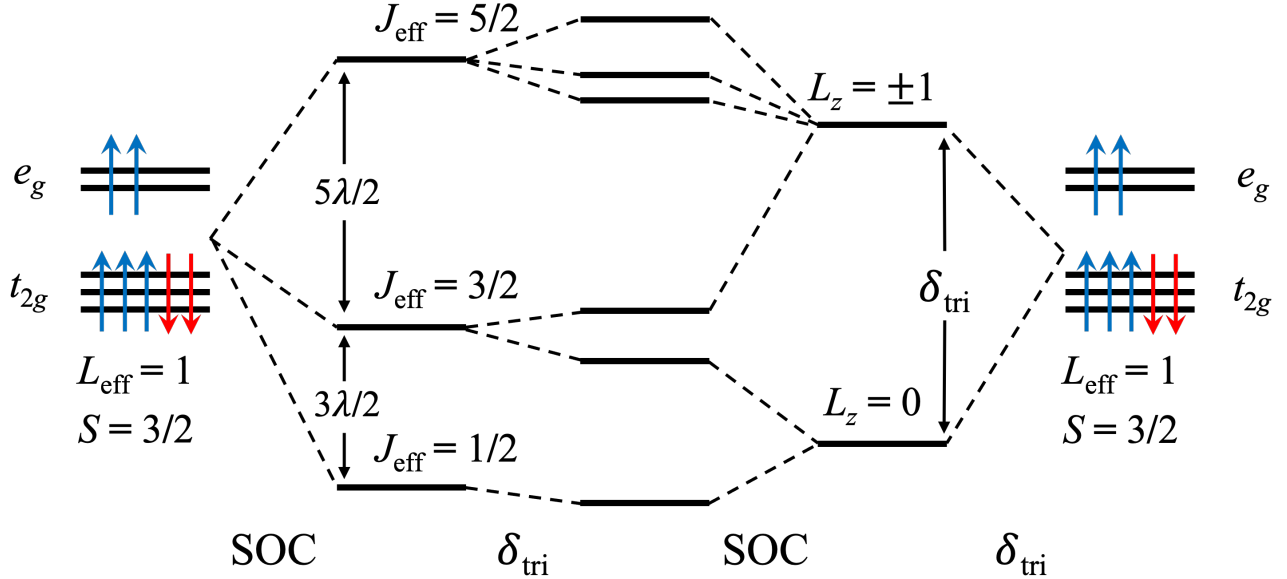


Fig. S2. Energy splitting of d^7 high spin state. The high spin state is 12-fold degenerate states with spin quantum number $S = 3/2$ and effective orbital quantum number $L_{\text{eff}} = 1$ on t_{2g} sub-shell. In strong SOC limit, the 12-fold degenerate states split into J_{eff} states with quantum number $J_{\text{eff}} = 1/2$, $J_{\text{eff}} = 3/2$ and $J_{\text{eff}} = 5/2$. The trigonal crystal field perturbation would further split J_{eff} degenerate states. In strong trigonal crystal field, the t_{2g} states split into a_{1g} and e_g^{π} states. For positive trigonal crystal field $\delta > 0$, the hole on t_{2g} sub-shell occupies a_{1g} state, leading to $L_z = 0$ ground state.

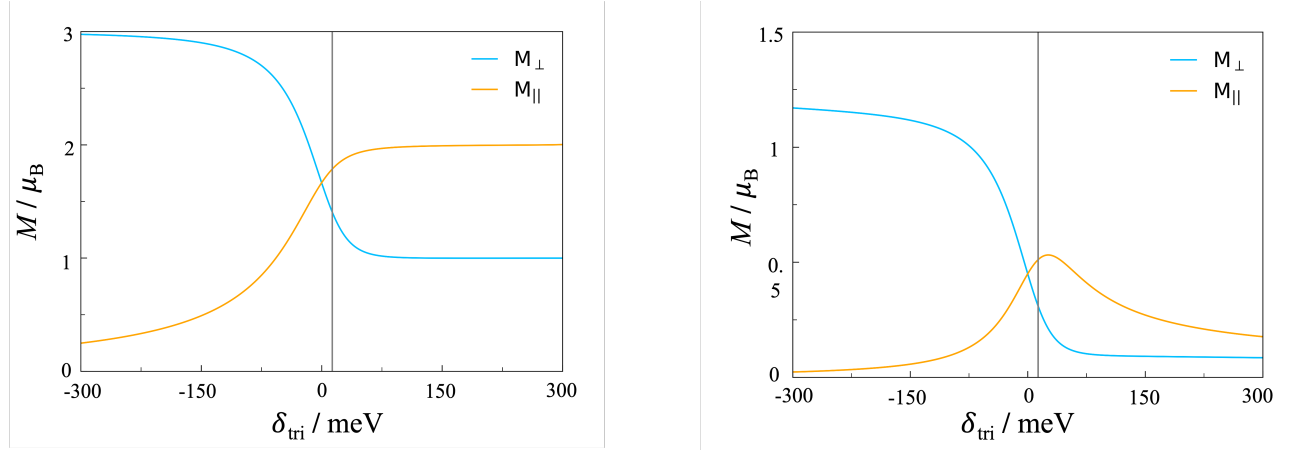


Fig. S3. Spin magnetic moment under different trigonal crystal field. The out-of-plane magnetic moment is denoted by blue curve while the in-plane magnetic moment is denoted by yellow curve. The gray line denotes realistic trigonal crystal field strength $\delta_{\text{tri}} = 3\delta = 13.2$ meV of CoI_2 .

II. Occupation and magnetic moment

The occupation and magnetic moment are calculated with ED method on one-site model. The one-site model contains crystal field term, Coulomb repulsion and SOC,

$$H_{\text{one}} = H_{\text{CF}} + H_U + H_{\text{SOC}}. \quad (\text{S18})$$

Fig. S4. Orbital magnetic moment under different trigonal crystal field. The out-of-plane magnetic moment is denoted by blue curve while the in-plane magnetic moment is denoted by yellow curve. The gray line denotes realistic trigonal crystal field strength $\delta_{\text{tri}} = 3\delta = 13.2$ meV of CoI_2 .

We approximate the Coulomb repulsion using the isotropic Kanamori form, with the intra-orbital Hubbard parameter U and Hund's coupling J_H . The inter-orbital Hubbard parameter U' is taken as $U' = U - 2J_H$ in its spherically symmetric form [39]. The Coulomb repulsion

term is written as

$$\begin{aligned}
H_U = & U \sum_{i,a} n_{i,a,\uparrow} n_{i,a,\downarrow} + (U' - J_H) \sum_{i,a < b, \sigma} n_{i,a,\sigma} n_{i,b,\sigma} \\
& + U' \sum_{i,a \neq b} n_{i,a,\uparrow} n_{i,b,\downarrow} - J_H \sum_{i,a \neq b} c_{i,a\uparrow}^\dagger c_{i,a\downarrow} c_{i,b\downarrow}^\dagger c_{i,b\uparrow} \\
& + J_H \sum_{i,a \neq b} c_{i,a\uparrow}^\dagger c_{i,a\downarrow}^\dagger c_{i,b\downarrow} c_{i,b\uparrow},
\end{aligned} \tag{S19}$$

where a and b are orbitals and σ and σ' are spin states. We take intra-orbital Hubbard $U = 4.0$ eV and Hund's coupling $J_H = 0.9$ eV as used in DFT calculation.

The SOC term $H_{\text{SOC}} = \lambda \mathbf{L} \cdot \mathbf{S}$, is written as single-particle form in calculation:

$$H_{\text{SOC}} = \zeta \sum_j \mathbf{l}_j \cdot \boldsymbol{\sigma}_j \tag{S20}$$

where $\zeta = 3\lambda = 0.08$ eV is the atomic SOC strength and j represents the holes. The one-site model is solved with ED method, and the ground state is projected onto $J_{\text{eff}} = 1/2$, $L_z = 0$ and $L_z = \pm 1$ states to obtain the occupation $|\langle \Psi_{\text{ground}} | J_{\text{eff}} = 1/2 \rangle|^2$, $|\langle \Psi_{\text{ground}} | L_z = 0 \rangle|^2$ and $|\langle \Psi_{\text{ground}} | L_z = \pm 1 \rangle|^2$. The magnetic moment is obtained by solving one-site model under a weak out-of-plane or in-plane Zeeman field. The ground state is used to calculate the expectation of total magnetic moment $\langle (\vec{L} + 2\vec{S}) \rangle$, spin magnetic moment $\langle 2\vec{S} \rangle$ and orbital magnetic moment $\langle \vec{L} \rangle$.

The spin magnetic moment, orbital magnetic moment and total magnetic moment are shown in Fig. S3, Fig. S4 and inset figure in Fig. 1(c). In the trigonal compression limit (left part of the figure), the ground state is characterized by $L_z = \pm 1$. Because of unquenched orbital magnetic moment in $L_z = \pm 1$ orbitals, the spin is constrained along z-axis, resulting in a negligible in-plane spin magnetic moment. Note that the orbital magnetic moment exceeding $1 \mu_B$ is caused by the finite crystal field Δ , leading to a non-zero occupation of the e_g^σ orbitals. In the trigonal elongation limit (right part of the figure), the ground state corresponds to $L_z = 0$. The orbital magnetic moment is quenched, leading to weak in-plane anisotropy. Consequently, the spin magnetic moment is primarily oriented in the in-plane direction. For SOC limit (middle part of the figure), the ground state is $J_{\text{eff}} = 1/2$ state. The $J_{\text{eff}} = 1/2$ is isotropic state, resulting in the same magnetic moment along any directions.

III. Wannier results

The Wannier function analysis is based on density functional theory (DFT) calculation. The DFT calculations are performed using Vienna Ab Initio Simulation Package (VASP) [49], within the framework of generalized gradient approximation (GGA) [50]. The kinetic energy cutoff of 500 eV and a Gamma centered k -mesh

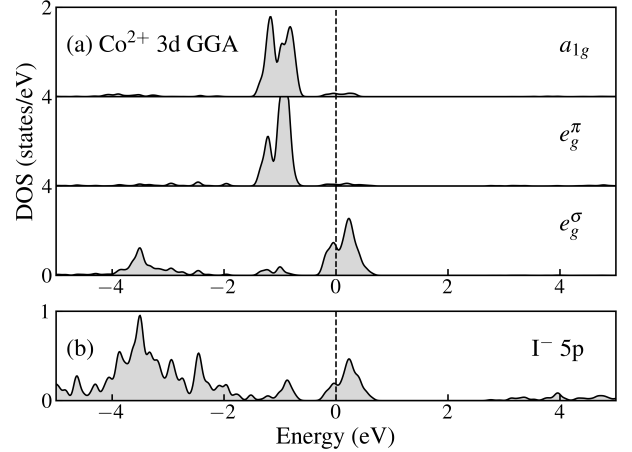


Fig. S5. (a) Co 3d and (b) I 5p density of states (DOS) from GGA calculation. The Fermi level is set at zero energy. The DOS of Co are projected to a_{1g} , e_g^π and e_g^σ orbitals, considering the triangular crystal field.

of $9 \times 9 \times 4$ are used for the unit cell. We use the $P\bar{3}m1$ crystal structure of CoI_2 [51]. And the lattice constants are optimized to be $a = b = 3.87 \text{ \AA}$ and $c = 7.06 \text{ \AA}$. In the structure optimization, all atoms are fully relaxed with the tolerance of 10^{-6} eV for total energy and 0.01 eV/\AA for atomic forces. As seen in Fig. S5, the a_{1g} and e_g^π states are nearly degenerate, suggesting a small trigonal crystal field.

We perform Wannier function analysis based on GGA result, using Wannier90 package [42]. To study magnetic properties of Co, we construct Wannier function based on Co d orbitals. As shown in Fig. S6, the Wannier functions band structure well reproduce the DFT band structure. To further check the reliability of Wannier function analysis, we plot Wannier function in Fig. S7. These Wannier functions are localized at Co ions with contribution from p orbitals of ligands, which results from p - d bonds and through which the indirect hopping processes are included in our model. Note that the hybridization between the e_g^σ orbitals and p orbitals is particularly strong, leading to significant e_g - t_{2g} hopping terms.

The crystal field term H_{CF} and hopping matrix $H_t^{(ij)}$ are obtained from Wannier function analysis. Here, we present the hopping matrices for the Z bond. The hopping matrices of X and Y bonds are related with Z bond matrices by C_3 rotation in the [111] direction. For CoI_2 , the crystal field term H_{CF} and hopping matrices between first nearest neighbors H_t^{1st} , second nearest neighbors H_t^{2nd} and third nearest neighbors H_t^{3rd} are (in meV)

$$H_{\text{CF}} = \begin{pmatrix} 5280.0 & 0 & -2.1 & -2.1 & 4.1 \\ 0 & 5280.0 & -3.6 & 3.6 & 0 \\ -2.1 & -3.6 & 4258.6 & 4.4 & 4.4 \\ -2.1 & 3.6 & 4.4 & 4258.6 & 4.4 \\ 4.1 & 0 & 4.4 & 4.4 & 4258.6 \end{pmatrix}, \tag{S21}$$

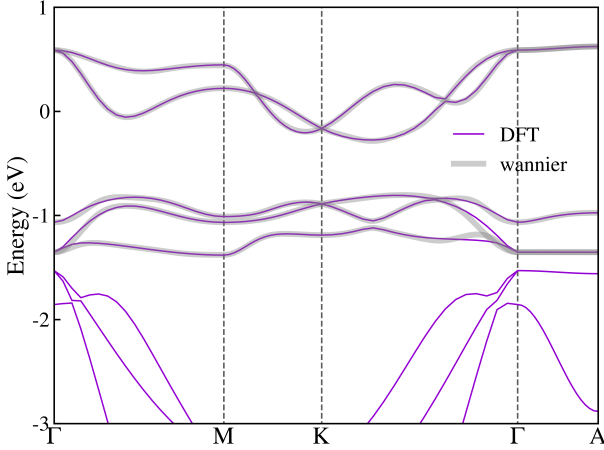


Fig. S6. Band structure from GGA calculation. The purple line and gray line represent DFT band structure and Wannier band structure respectively.

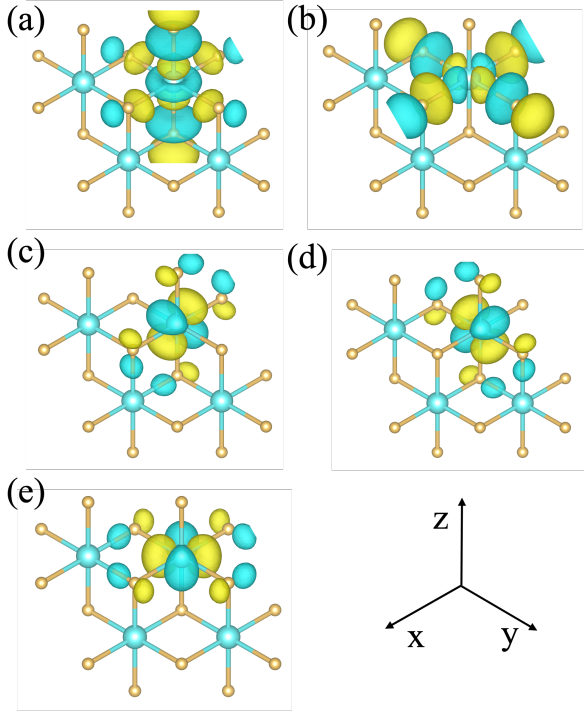


Fig. S7. Contour-surface plots of Co (a) $d_{3z^2-r^2}$, (b) $d_{x^2-y^2}$, (c) d_{xz} , (d) d_{yz} and (e) d_{xy} Wannier functions.

$$H_t^{1st} = \begin{pmatrix} 18.1 & 0 & 10.3 & 10.3 & 177.1 \\ 0 & 22.6 & 5.3 & -5.3 & 0 \\ 10.3 & 5.3 & 29.2 & 24.7 & 5.1 \\ 10.3 & -5.3 & 24.7 & 29.2 & 5.1 \\ 177.1 & 0 & 5.1 & 5.1 & -44.1 \end{pmatrix}, \quad (S22)$$

$$H_t^{2nd} = \begin{pmatrix} -14.0 & 0 & -11.8 & -11.8 & 39.6 \\ 0 & 7.8 & 2.9 & -2.9 & 0 \\ -11.8 & 2.9 & -0.7 & -39.1 & 3.2 \\ -11.8 & -2.9 & -39.1 & -0.7 & 3.2 \\ 39.6 & 0 & 3.2 & 3.2 & 2.6 \end{pmatrix}, \quad (S23)$$

$$H_t^{3rd} = \begin{pmatrix} -44.0 & 0 & -5.8 & -5.8 & 20.9 \\ 0 & 92.0 & -4.5 & 4.5 & 0 \\ -5.8 & -4.5 & 8.1 & -5.3 & 5.6 \\ -5.8 & 4.5 & -5.3 & 8.1 & 5.6 \\ 20.9 & 0 & 5.6 & 5.6 & -32.7 \end{pmatrix}. \quad (S24)$$

For $\text{Co}_{2/3}\text{Mg}_{1/3}\text{I}_2$, the crystal field term H_{CF} and hopping matrices between first nearest neighbors H_t^{1st} , second nearest neighbors H_t^{2nd} and third nearest neighbors H_t^{3rd} are (in meV)

$$H_{\text{CF}} = \begin{pmatrix} 4659.8 & 0 & 4.6 & 4.6 & -9.2 \\ 0 & 4659.8 & 8.0 & -8.0 & 0 \\ 4.6 & 8.0 & 3671.2 & 1.5 & 1.5 \\ 4.6 & -8.0 & 1.5 & 3671.2 & 1.5 \\ -9.2 & 0 & 1.5 & 1.5 & 3671.2 \end{pmatrix}, \quad (S25)$$

$$H_t^{1st} = \begin{pmatrix} 12.2 & 0 & 9.9 & 9.9 & 148.0 \\ 0 & 58.8 & 0.3 & -0.3 & 0 \\ 9.9 & 0.3 & 17.4 & 32.0 & -5.1 \\ 9.9 & -0.3 & 32.0 & 17.4 & -5.1 \\ 148.0 & 0 & -5.1 & -5.1 & -2.7 \end{pmatrix}, \quad (S26)$$

$$H_t^{2nd} = \begin{pmatrix} -1.6 & -4.7 & -11.7 & -13.4 & 38.0 \\ 4.7 & 2.8 & -1.5 & -0.1 & 7.3 \\ -13.4 & 0.1 & -1.7 & -41.4 & 7.7 \\ -11.7 & 1.5 & -29.2 & -1.7 & 0.1 \\ 38.0 & -7.3 & 0.1 & 7.7 & -0.3 \end{pmatrix}, \quad (S27)$$

$$H_t^{3rd} = \begin{pmatrix} -25.2 & 0 & -6.6 & -6.6 & 19.3 \\ 0 & 47.9 & -3.8 & 3.8 & 0 \\ -6.6 & -3.8 & 4.9 & -7.1 & 9.4 \\ -6.6 & 3.8 & -7.1 & 4.9 & 9.4 \\ 19.3 & 0 & 9.4 & 9.4 & -31.4 \end{pmatrix}. \quad (S28)$$

IV. Exchange parameters

We obtained the exchange parameters by solving two-site Hubbard model,

$$H = H_{\text{one}} + H_t, \quad (S29)$$

where the crystal field terms and hopping terms are obtained through Wannier function analysis.

We used exact diagonalization and projection to obtain the exchange parameters. Technically, our approach

begins with the exact diagonalization of the Hubbard model to obtain the four lowest-energy eigenstates, denoted as $|n\rangle$, along with their corresponding energy spectrum. We then define a target subspace spanned by the pure $J_{\text{eff}} = 1/2$ basis states, $|n_l\rangle$. To derive the effective Hamiltonian, the low-energy eigenstates $|n\rangle$ are first projected onto the subspace spanned by $|n_l\rangle$. Subsequently, we apply Löwdin symmetric orthonormalization to construct a set of orthonormal basis states, and at the same time the diagonalized energy spectrum is transformed into effective Hamiltonian. This exact diagonalization and projection scheme is identical to the methodology employed for the calculations of Na_2IrO_3 and RuCl_3 [45].

The Hubbard model is solved by ED method and the obtained four lowest eigenstates are $|J_{\text{eff}} = \frac{1}{2}, J_{\text{eff}} = \frac{1}{2}\rangle$, $|J_{\text{eff}} = \frac{1}{2}, J_{\text{eff}} = -\frac{1}{2}\rangle$, $|J_{\text{eff}} = -\frac{1}{2}, J_{\text{eff}} = \frac{1}{2}\rangle$ and $|J_{\text{eff}} = -\frac{1}{2}, J_{\text{eff}} = -\frac{1}{2}\rangle$. Due to the limited trigonal crystal field, the $J_{\text{eff}} = \frac{1}{2}$ eigenstates are mixed with $J_{\text{eff}} = \frac{3}{2}$ and $J_{\text{eff}} = \frac{5}{2}$ states, as shown in Fig. S2. As we show in main texture, the occupation of $J_{\text{eff}} = \frac{1}{2}$ is over 0.98 and the majority of eigenstate is still $J_{\text{eff}} = \frac{1}{2}$ state.

To study contributions from each channel, we calculated the dependence of Heisenberg interaction J and Kitaev interaction K on each hopping channel, as shown in Fig. S8. For first nearest neighbors, the strongest channel is $t_{2g}-e_g$ hopping term $t_6 = 177.1$ meV. And the single channel contributions in CoI_2 are listed in Table S1. The t_6 channel contributes a AFM Heisenberg interaction $J = 0.81$ meV and a FM interaction $K = -4.73$ meV. In the meantime, the $t_3 = -44.1$ meV channel contributes a AFM Kitaev interaction $K = 0.03$ meV and a FM Heisenberg interaction $J = -0.15$ meV. For second nearest neighbors, the $t_{2g}-t_{2g}$ hopping term $t_2 = -39.1$ meV contributes a FM Heisenberg interaction $J = -0.24$ meV and a FM Kitaev interaction $K = -0.26$ meV. And the $t_{2g}-e_g$ hopping term $t_6 = 39.6$ meV contributes a AFM Heisenberg interaction $J = 0.05$ meV and a FM Kitaev interaction $K = -0.22$ meV. For third nearest neighbors, the strongest hopping channel is e_g-e_g hopping channel $t_4 = 92.0$ meV. The t_4 channel contributes a AFM Heisenberg interaction $J = 1.9$ meV and a FM Kitaev interaction $K = -0.05$ meV. The t_4 channel results the AFM Heisenberg interaction between third nearest neighbors.

Table S1. Magnetic interactions (meV) from each single channel for CoI_2 between first, second and third nearest neighbors.

		J	K	Γ	Γ'
1NN	t_1	-0.10	0.12	-0.01	0.01
	t_2	-0.10	-0.10	-0.00	-0.03
	t_3	-0.15	0.03	-0.03	-0.02
	t_4	0.12	-0.00	0.02	0.01
	t_5	0.08	-0.00	0.01	0.01
	t_6	0.81	-4.73	0.17	-0.22
2NN	t_1	-0.00	0.00	-0.00	0.00
	t_2	-0.24	-0.26	-0.01	-0.08
	t_3	-0.00	0.00	-0.00	-0.00
	t_4	0.01	-0.00	0.00	0.00
	t_5	0.05	-0.00	0.01	0.01
	t_6	0.05	-0.22	0.01	-0.01
3NN	t_1	-0.01	0.01	-0.00	0.00
	t_2	-0.00	-0.00	-0.00	-0.00
	t_3	-0.08	0.02	-0.01	-0.00
	t_4	1.90	-0.05	0.34	0.26
	t_5	0.44	-0.01	0.07	0.06
	t_6	0.02	-0.06	0.00	-0.00

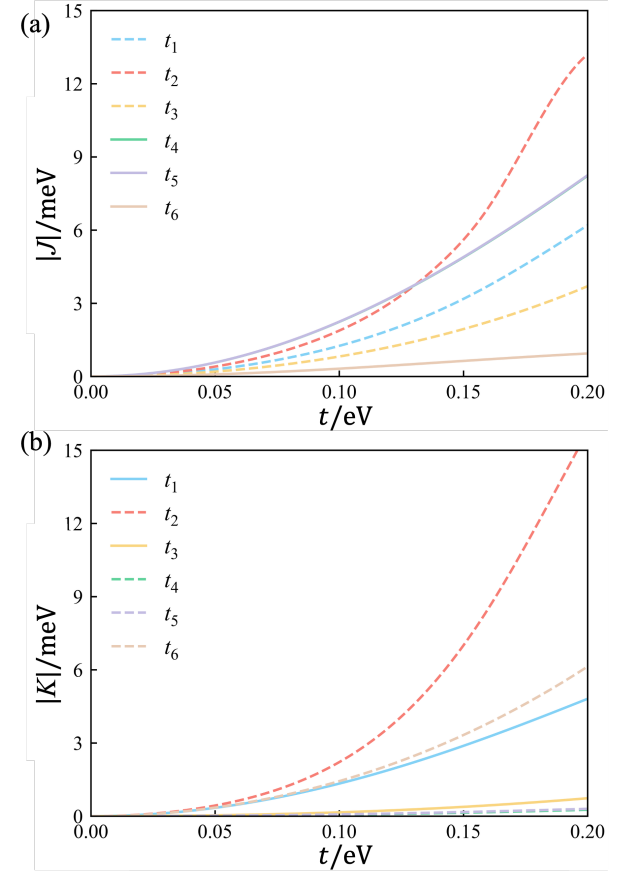


Fig. S8. The dependence of the exchange interaction on the hopping terms t_{1-6} : (a) Heisenberg interaction J , (b) Kitaev interaction K . The dash line and solid line indicate FM interaction and AFM interaction, respectively.

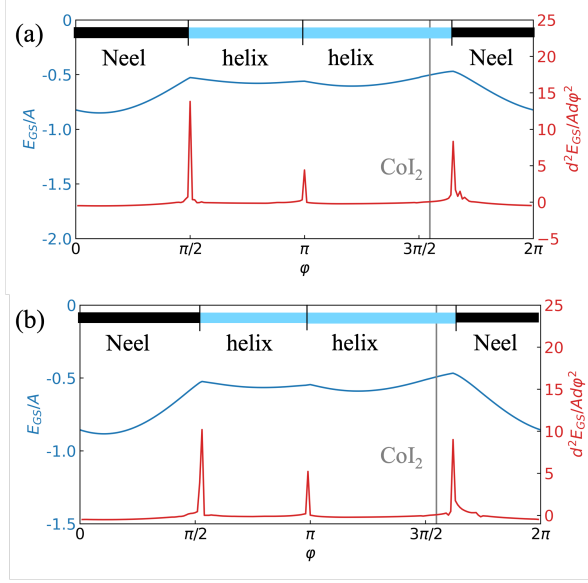


Fig. S9. Phase diagram of (a) J_1 - K_1 - J_3 model and (b) J_1 - K_1 - J_2 - J_3 model.

V. Magnetic structure

We calculate the ground state of the spin model using density matrix renormalization group (DMRG) method [52] implemented in the ITensor library [53] for triangular lattice and ED method for hexagonal lattice. For triangular lattice, we performed DMRG calculations on a 6×6 lattice with periodic boundary conditions, performing over 10 sweeps with up to 1600 states in each DMRG block. For hexagonal lattice, we used ED method to calculate the ground state on a 6×4 lattice.

Here we also calculated the phase diagram for the triangular lattice with the model containing interactions between first, second and third nearest neighbors. As shown in Fig. S9, the phase diagram is almost identical to the one without the second nearest neighbor interaction, due to the very weak J_2 interaction. Therefore, in our calculation of geometric frustration, only J_3 is considered significant.

To determine the ground state, we calculated the magnetic structure factor $S(q)$,

$$S(q) = \frac{1}{N} \sum_{ij} S_i S_j e^{i\vec{q} \cdot \vec{R}_{j-i}}, \quad (\text{S30})$$

where S_i and S_j are spin moment expectation of site i and site j , N is the number of sites and \vec{R}_{j-i} is displacement between site i and site j in real space. The magnetic structure factor of triangular lattice is shown in Fig. S10.

The magnetic structure factor $S(q)$ of $\text{Co}_{2/3}\text{Mg}_{1/3}\text{I}_2$ displays the sequence of phase transition associated with J_3 interaction. As shown in Fig. S11(a), without J_3 , $S(q)$ displays sharp peak at M -point in second Brillouin zone, which corresponds to stripe AFM order. In Fig.

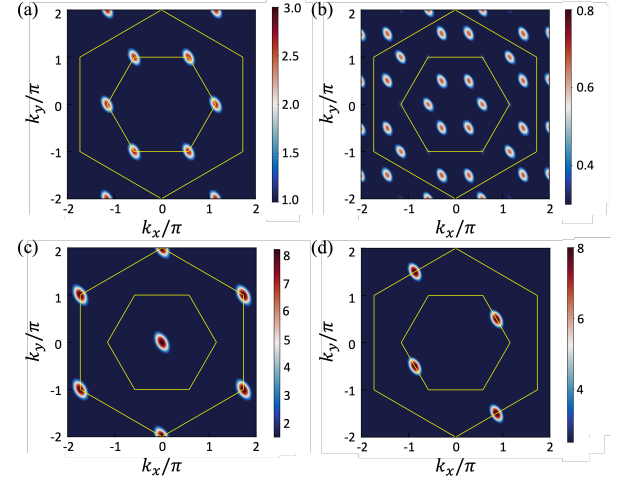


Fig. S10. Magnetic structure factor $S(q)$ of (a) 120° Neel AFM state, (b) helical AFM state, (c) FM state and (d) stripe AFM state.

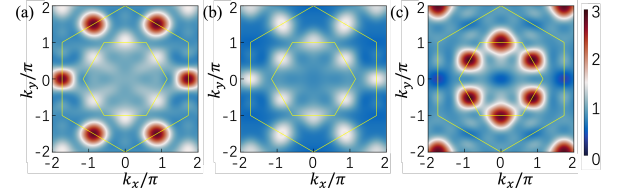


Fig. S11. Magnetic structure factor $S(q)$ of $\text{Co}_{2/3}\text{Mg}_{1/3}\text{I}_2$ with (a) 0% J_3 , (b) 30% J_3 , (c) 100% J_3 . The colormap is limited to the range of 0 to the maximum value $S(q)_{\text{max}}$ of zigzag and stripe order.

S11(b), a limited J_3 induces diffused $S(q)$ with soft peak at M -point in first and second Brillouin zone. And as shown in Fig. S11(c), where J_3 is relatively strong, $S(q)$ displays sharp peak at M -point in first Brillouin zone and the ground state is zigzag AFM.

To assess the robustness of our conclusions, we performed a sensitivity analysis on Wannier-based extraction of crystal fields, Δ and δ , and the selection of λ , U and J_H , by changing each parameters by 10% as illustrated in S12. We find that the variation does not affect our conclusion.

To determine the Kitaev QSL phase in Fig. S12, we calculated the magnetic structure factor $S(q)$ of pure Kitaev model, as shown in S13(a), and plaquette operator $\langle W_p \rangle$ in the phase diagram, as shown in S13(b), via exact diagonalization method. The plaquette operator $\langle W_p \rangle$ is defined as the product of spin components around a hexagonal plaquette $W_p = 2^6 S_1^x S_2^y S_3^z S_4^x S_5^y S_6^z$, where the specific spin component at each site corresponds to the bond direction external to the loop, to characterize the Kitaev QSL[4]. The lack of distinct peaks in Fig. S13(a) and the computed values of $\langle W_p \rangle$ in Fig. S13(b) confirm the Kitaev QSL phase.

To investigate the magnetic field response of

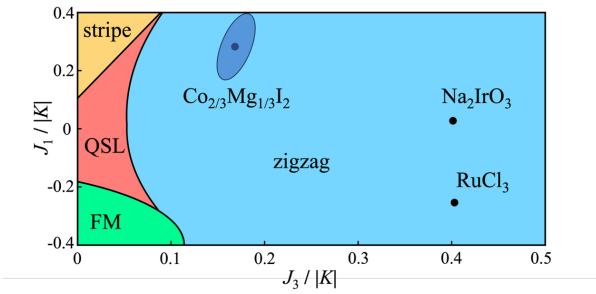


Fig. S12. Sensitivity of the $\text{Co}_{2/3}\text{Mg}_{1/3}\text{I}_2$ phase region to parameter variations. The dark blue area indicates the confidence interval for the $\text{Co}_{2/3}\text{Mg}_{1/3}\text{I}_2$ phase.

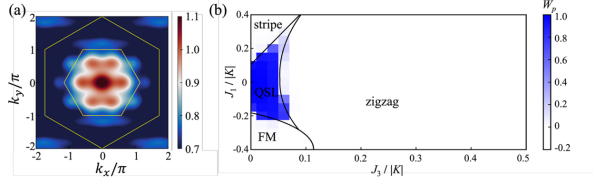


Fig. S13. (a) Magnetic structure factor of QSL region and (b) Phase diagram, obtained via exact diagonalization. The color scale indicates the expectation value of (a) magnetic structure factor, and (b) the plaquette operator $\langle W_p \rangle$.

$\text{Co}_{2/3}\text{Mg}_{1/3}\text{I}_2$, we incorporated the Zeeman term into the spin Hamiltonian as $H_Z = g_{\perp}\mu_B\mathbf{B}\mathbf{S}$, where g_{\perp} denotes the out-of-plane g factor and μ_B is the Bohr magneton. As seen in Fig. S14, our calculations find that the Kitaev QSL phase emerges within the intermediate magnetic field of 2.0–4.3 T.c

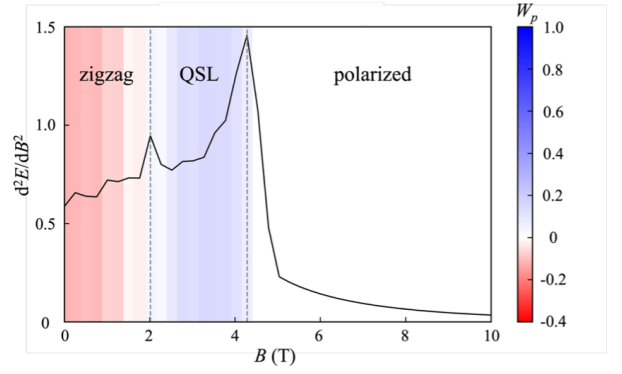


Fig. S14. Phase diagram of $\text{Co}_{2/3}\text{Mg}_{1/3}\text{I}_2$ obtained via exact diagonalization under external magnetic field. The color scale indicates the expectation value of the plaquette operator $\langle W_p \rangle$.